communications physics

A Nature Portfolio journal

Article

https://doi.org/10.1038/s42005-025-02267-y

Valley resolved dynamics of phonon bottleneck in semiconductor molybdenum ditelluride

Zhong Wang[1,2], Yijie Shi[1,2], Yu Pan[3], Min Li[4], Xi Wang[1,2], Zheng Zhang[1,2], Xiangyu Zhu[1,2], Fuyong Hua[1,2], Qian You[1,2,5], Chunlong Hu[1,2], Junjie He[4], Yu Ye[3] & Wenxi Liang[1,2]

Semiconductor molybdenum ditelluride (2H-$MoTe_2$) possess multiple valleys in the band structure, enriching its physical properties and potentials in applications. However, the effect of multiple valleys on the mechanisms of population and relaxation of carriers and phonons remains limited, particularly due to the inadequacy of current optical probes that lack momentum sensitivity. Here, we rely on time resolved measurements of optical absorption and electron diffraction to investigate the carrier intra- and intervalley scattering and the phonon dynamics in different valleys in photoexcited few-layer 2H-$MoTe_2$. Our experimental results are complemented by density functional theory calculations and molecular dynamics simulations. We reveal the pathways and timescales of carrier relaxation, accompanied with the emissions of optical phonons at the Brillouin zone center and acoustic phonons at the zone border. We estimate the population of different phonon modes based on the measured results, identifying quantitatively the occurrences of phonon bottleneck located in different valleys. Our technique allows constructing a comprehensive picture of the complex interactions between carriers and phonons in 2H-$MoTe_2$ with the valley degree of freedom resolved.

Molybdenum ditelluride ($MoTe_2$) with three crystal phases[1] of semiconducting 2H, semimetallic 1T′, and type-II Weyl semimetallic T_d, offers an ideal platform material for studying the attractive family of transition metal dichalcogenides (TMDCs), which possesses abundant physical phenomena, e.g., charge density wave[2], superconductivity[3], and topological electronic phase[4]. In terms of applicability, 2H-$MoTe_2$ is potentially compatible with the mature silicon-based industry[5] due to its tunable bandgap of ~1 eV, close to that of silicon, and has been implemented in various applications[6], including the third generation solar cells[7], valleytronic devices[8], highly sensitive photodetectors[9], and phase-change memories[10]. The carrier and lattice dynamics of 2H-$MoTe_2$, which link the properties to the physical phenomena and device performances, have been studied through multiple time-resolved approaches[7,11–14]. But the complexity of microscale processes involving time spans, pathways, and interactions induced by the valley degree of freedom is yet to be elucidated, as the excited carriers in TMDCs evolve under the basic frame of intra- and intervalley scattering[15].

For the carrier relaxation in 2H-$MoTe_2$, the exciton dynamics have been extensively investigated, yielding quantitative results, e.g., the carrier multiplication in hundreds of femtoseconds[7] and the defect-assisted non-radiative recombination of band-edge excitons in a few picoseconds[14]. Optical probe is currently the main approach to examine carrier dynamics, but the information obtained so far is inadequate to provide a comprehensive understanding for clarifying the mechanisms of electron-phonon scattering during non-radiative energy transfer[16], and especially for achieving a consensus on the conflicting observations. For example, the observations of core-level spectroscopy[13] and X-ray spectroscopy[12] found that the hot carriers, which have a critical impact on photovoltaics, relax to the band edge within hundreds of femtoseconds, but the details of the cooling path are still ambiguous. The study of lattice dynamics showed that the hot and band-edge electrons preferentially coupled to optical (OPs) and acoustic phonons (APs)[11], respectively, but the latter is inconsistent with the observed A_{1g} phonon under infrared excitation[17]. The reported strong electron-phonon coupling[18] probably conflicts with some higher-order coupling within carriers, such as the impact ionization, contradicting the high conversion efficiency of carrier multiplication[7]. Among all complex dynamics, the carrier migration path within multiple valleys and the role of

[1]Wuhan National Laboratory for Optoelectronics, Huazhong University of Science and Technology, 1037 Luoyu Road, Wuhan, 430074, China. [2]Advanced Biomedical Imaging Facility, Huazhong University of Science and Technology, Wuhan, 430074, China. [3]State Key Laboratory for Mesoscopic Physics and Frontiers Science Center for Nano-Optoelectronics, School of Physics, Peking University, Beijing, 100871, China. [4]Department of Physical and Macromolecular Chemistry, Faculty of Science, Charles University, Prague, 12843, Czech Republic. [5]Present address: Zhongshan Lighting Fast Intellectual Property Rights Service Center, Zhongshan, 528421, China. e-mail: wxliang@hust.edu.cn

different phonon modes involved are of particular interest, due to the hot topic of valleytronics in developing novel photoelectronics. To resolve the dynamics with multiple valleys in the band structure, the methodology with momentum sensitivity is demanded.

In this work, we investigate the energy relaxation carried by carriers and phonons in monocrystalline 2H-$MoTe_2$, through the combination of pump–probe based transient absorption (TA) spectroscopy and ultrafast electron diffraction (UED), and the density functional theory calculation and non-adiabatic molecular dynamics (NAMD) simulation. The relaxations of hot carriers and band-edge excitons, and the population and decoherence of OPs revealed by TA and NAMD, together with the momentum-resolved evolutions of strongly coupled phonon (SCP) observed by UED, construct the scenario of intra- and intervalley carrier scattering with dominating OPs at the Brillouin zone (BZ) center and APs at the BZ border, followed by the rapid lattice disorder before the completion of thermalization. With the computations of phonon population based on the results of time-resolved measurements, the phonon bottlenecks retarding the cooling processes of hot carriers are quantitatively identified in different valleys.

Results

The 2H-$MoTe_2$ films with thickness of 6–7 nm (9–10 atomic layers) were epitaxially grown on a silicon wafer (see Methods)[19], then transferred onto bare grid as the free-standing (FS) specimen, and onto carbon membrane coated grid as the carbon-membrane-supported (CS) specimen with a heterostructure interface, as shown in Fig. 1a. The pump-probe setup of TA and UED is schematically illustrated in Supplementary Fig. 2. The hexagonal lattice structure and the diffraction pattern with four families of crystallographic plane recorded by UED are shown in Fig. 1a, b, respectively. We computed the electronic band structure and electronic density of states using the Vienna Ab initio Simulation Package code (see Methods)[20], as depicted in Fig. 1c, showing the valence band maximum and the conduction band minimum (CBM) located at the Γ and Λ points of the BZ, respectively. The TA results measured in the 450–1400 nm region (see Methods) with excitation fluence of 90 μJ cm^{-2} are presented in Fig. 1d, showing the photo-induced bleach peaks at 1230 nm (PIB-A), 950 nm (PIB-B), 736 nm (PIB-A′), and 607 nm (PIB-B′), which rise from the exciton transitions split by spin–orbit coupling at the K and Γ points, together with the peak at 501 nm (PIB-C) from the direct bandgap transition at the Γ point[21].

Hot carrier relaxation

We focus on the kinetics of PIB-C and PIB-A to examine the relaxations of hot carriers and band-edge excitons. The decay of PIB-C is well fitted by a tri-exponential function (see Supplementary Fig. 3) with characteristic times of 0.8, 5.7, and 517.6 ps, as depicted in Fig. 2a, denoting the cooling of excited electrons from the Γ point populating at the border of Λ valleys. The 0.8 ps decay is attributed to the spontaneous relaxation of hot electrons, which are described as intravalley scattering[22] toward the valley bottom, accompanied by the multiple emissions of OPs near the BZ center. One SCP mode can

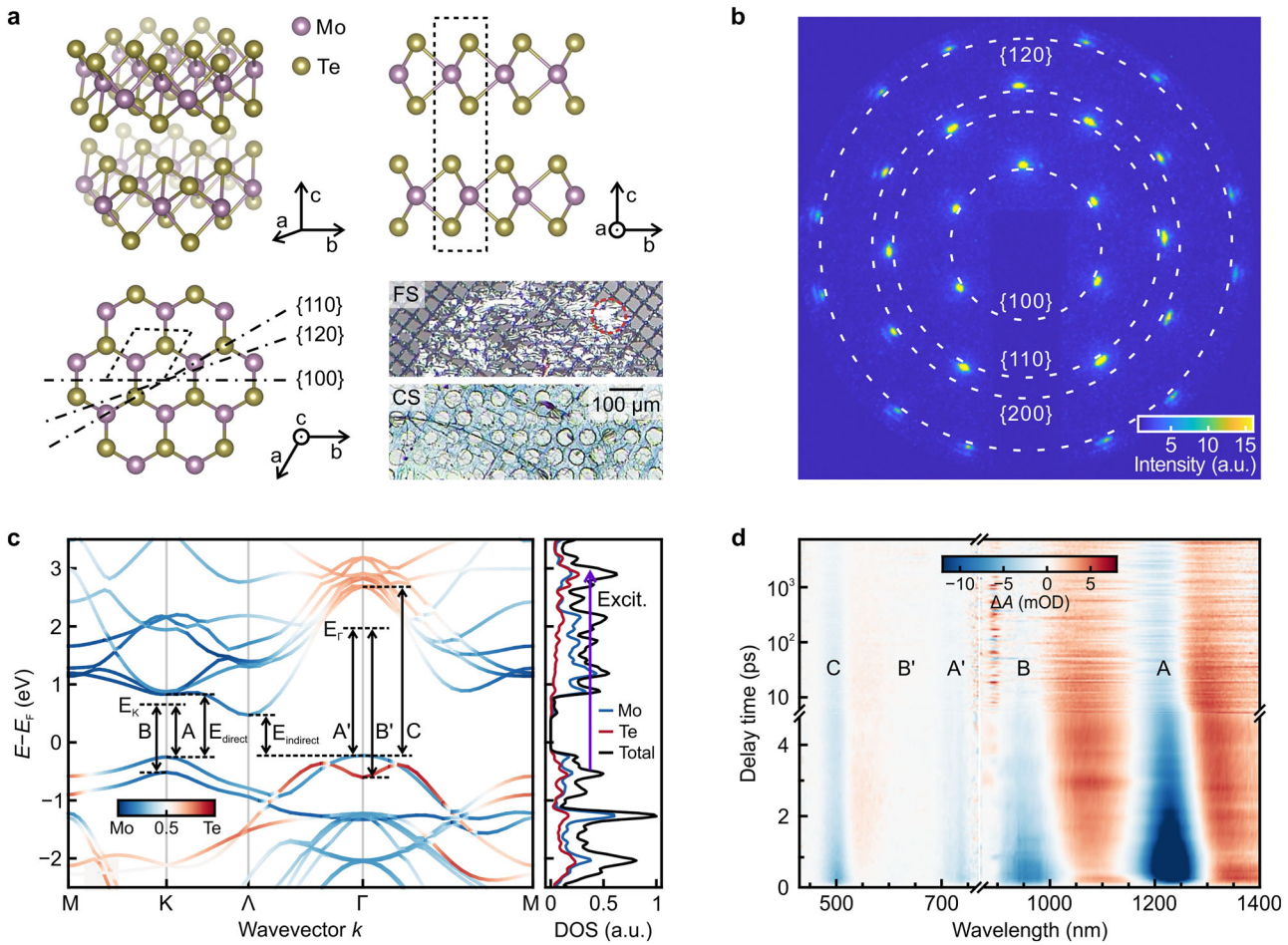

Fig. 1 | Specimens, lattice and band structures, and ultrafast electron diffraction and transient absorption results. a Hexagonal lattice of 2H-$MoTe_2$ with a layered structure bonding by van der Waals force, marked with the projections of the crystallographic plane (dash-dot lines) recorded in UED. Dashed frames, unit cell. Inset, optical photographs of the free-standing (FS) and carbon-membrane-supported (CS) specimens, marked with the probed area (dashed red circle). **b** UED diffraction pattern containing Bragg spots of four families of crystallographic planes parallel to the c-axis. **c** Calculated electronic band structure. Inset, density of states (DOS) for bulk 2H-$MoTe_2$, marked with the transition energies upon above-bandgap excitation (400 nm, purple arrow) probed in TA. **d** Pseudocolor contour plot of the TA spectrum in the visible–infrared wavelength range, showing photo-induced bleach peaks corresponding to the transitions marked in (**c**).

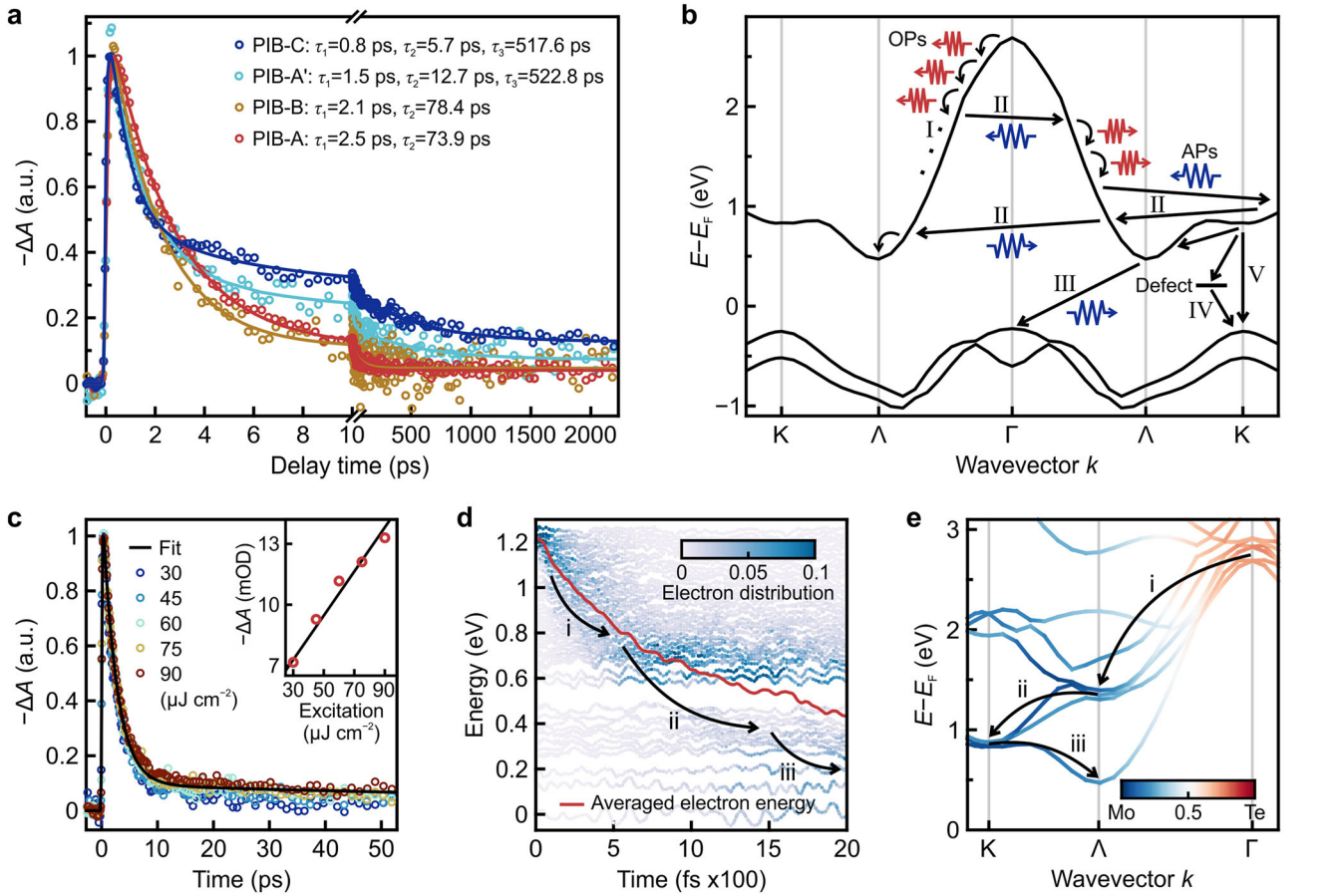

Fig. 2 | Transient absorption measured carrier relaxations and non-adiabatic molecular dynamics simulations. a Normalized decay of photo-induced bleach peaks. Solid lines, multiexponential fits. **b** Schematic illustration of carrier relaxation pathways in the simplified electronic bands. I, intravalley scattering accompanied by the emission of optical phonons (OPs, red). II, intervalley scattering accompanied by the emission of acoustic phonons (APs, blue). III, indirect recombination. IV, defect-assisted recombination. V, direct recombination. **c** Normalized decays of PIB-A under various excitation fluences, with a biexponential fit. Inset, linear dependence of bleach amplitude on excitation fluence. **d** Simulated three-stage energy decay of Γ_e. Processes i–iii, see Supplementary Note 1. **e** Cooling pathways of Γ_e in the conduction band at 0 K, concluded from the NAMD simulations. i, intravalley scattering in the Λ valley. ii and iii, intervalley scattering between the Λ and K valleys.

dominate the electron–phonon scattering during intraband relaxation in TMDCs, giving rise to the phonon cascade[23], which is common in semiconductors[24], as the process I illustrated in Fig. 2b. The longer lifetime compared to the few-hundred femtoseconds reported for MoS_2[25] is probably elongated by the phonon bottleneck originating from the phonon cascade. Based on the computed phonon dispersion curve, the highest energy of OPs at the Γ point is less than 40 meV (see Supplementary Fig. 4). Given that the energy span between the hot electrons and the Λ valley bottom is more than 1 eV, one electron needs to emit more than 25 phonons to relax to the CBM, with the emission (Γ_{em}) and absorption (Γ_{abs}) rates of a phonon mode as[26]

$$\Gamma_{em} \sim N_P + 1 \quad (1)$$

$$\Gamma_{abs} \sim N_P \quad (2)$$

where N_P is the population. These two rates become comparable when the population is pronouncedly larger than 1, resulting in the abundant nonequilibrium OPs emitted during phonon cascade, which in turn facilitate the reabsorption of phonons by the carriers, consequently retarding the carrier relaxation, i.e., the occurrence of phonon bottleneck.

The 5.7 ps decay is attributed to the intervalley scattering, because the six Λ valleys with surrounding satellite valleys in the CBM limit the wavevector of phonons participating in the carrier scattering, thus the phonon cascade can be interrupted only by scattering with the phonons with large enough wavevector, as the process II in Fig. 2b. The carrier cooling is possibly further slowed down effectively due to the electron storing in the satellite valleys for several picoseconds, consistent with the reported intervalley scattering of picoseconds[27] dominated by APs[28] in MoS_2. The last decay of 517.6 ps is attributed to the carrier recombination and diffusion, which are also reported with similar timescale in MoS_2[29]. This decay is represented by the indirect recombination of band-edge excitons, as the process III in Fig. 2b, impacting the carrier relaxation through Pauli blocking[27].

PIB-A decays with two processes of 2.5 and 73.9 ps. The absence of sub-picosecond process reflects no intravalley scattering for the band-edge A excitons, which populate at the bottom of K valleys. In the single particle picture, electrons at K valleys can relax to the Λ valleys though intervalley scattering. Thus the direct A excitons probably relax to indirect excitons through exciton–phonon scattering[30], forming K–Λ excitons because the bottom of Λ valley is the CBM. Such relaxations are consistent with the reduced quantum yield of photoluminescence[31]. The amplitudes of PIB-A show a linear dependence on excitation fluence, as depicted in the inset of Fig. 2c, indicating the high-order interactions such as Auger process did not play a significant role in our measurements. We therefore attributed the 2.5 ps decay to the contributions majorly from the intervalley scattering due to the low density of defect in the monocrystalline specimens, and partially from the defect-assisted nonradiative recombination[14] which is illustrated as the process IV in Fig. 2b. The 73.9 ps decay is attributed to the exciton lifetime, consistent with the reported rate of direct electron–hole recombination in other TMDCs[32], as the process V in Fig. 2b.

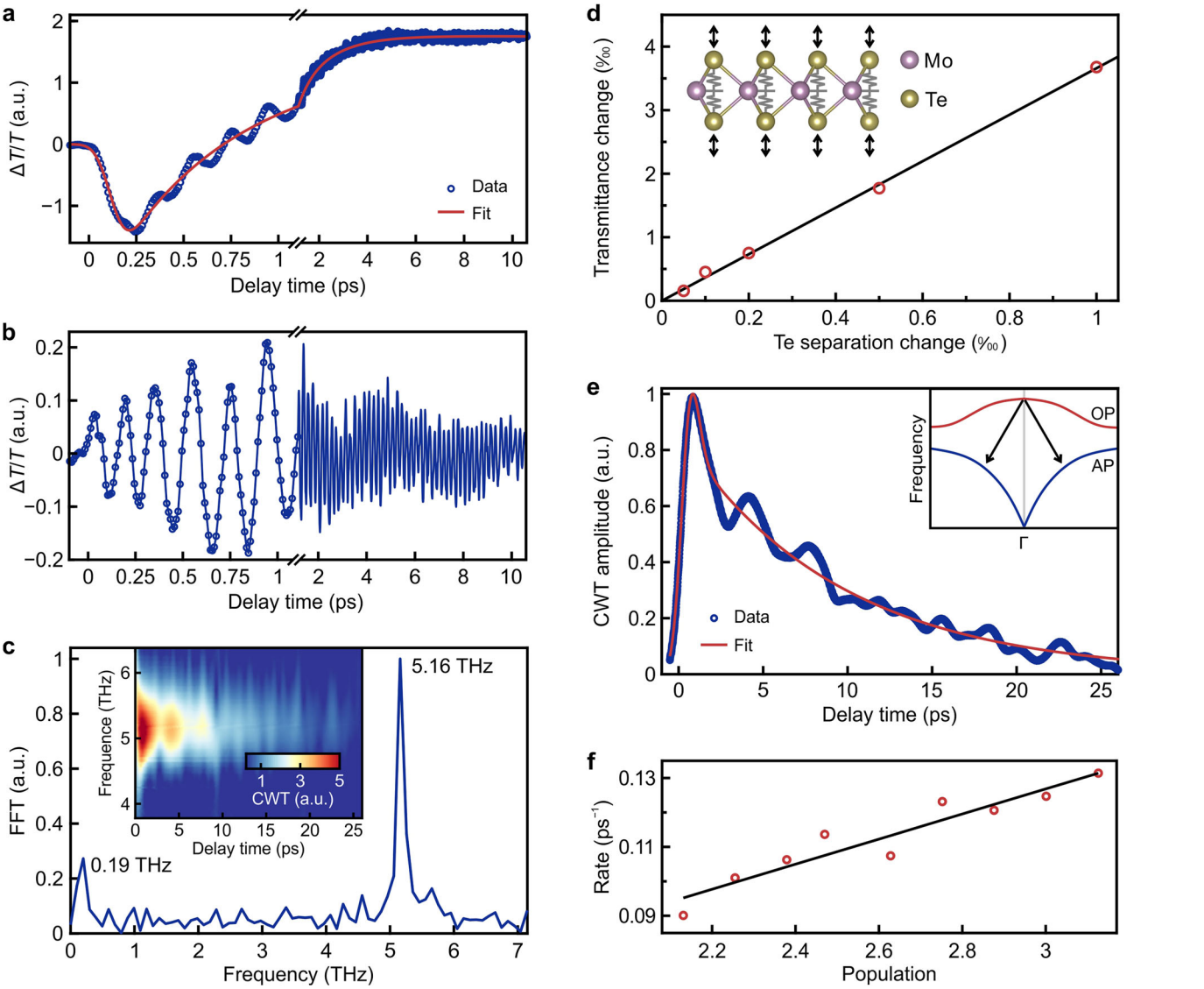

Fig. 3 | Population and decay of coherent phonons. a Temporal trace of transmission change and **b** the extracted oscillation signals, measured under 400 nm excitation with fluence of 90 μJ cm^{-2}. Only the kinetics within 10 ps are shown for clarity. **c** Breathing mode of 0.19 THz and A_{1g} mode of 5.16 THz extracted from **a** by fast Fourier transform (FFT). Inset, continuous wavelet transform (CWT) of the A_{1g} mode in (**b**). **d** Simulated linear dependence of transmittance changes on the separation changes of Te pairs, taking into account that the Te atoms vibrate along the out-of-plane direction while the Mo atoms keep still in A_{1g} mode, as illustrated in the inset. **e** Two-stage decay of A_{1g} mode extracted from the inset in (**c**), with biexponential fit. Inset, the Klemens channel for OPs decaying. **f** Linear dependence of the extracted anharmonic rate on the calculated population of low-frequency APs.

The concluded relaxation pathways of photoexcited carriers are corroborated by the NAMD simulations (see Methods) of the cooling and recombination of an electron with the lowest energy (Γ_e) and a hole with the second-lowest energy (Γ_h), at the Γ points in conduction and valence bands, respectively. The simulations reveal the carrier transfers between Te and Mo atoms, and the intra- and intervalley scattering of Γ_e and Γ_h, accompanied with the emission of A_{1g} phonons. A three-stage energy decay is found for Γ_e, as depicted in Fig. 2d, confirming the observed kinetics of PIB-C. The energy decay, together with the averaged coupling along NAMD trajectory and the time-dependent spatial localization, establish the scenario of Γ_e cooling with accurate band structure, as illustrated in Fig. 2e, well reproducing the pathways deduced from TA measurements, see Supplementary Note 1 for details.

Coherent phonon dynamics

We employed the high sensitivity of transient absorption measured with single-wavelength (see Methods) to track the coherent phonons, which modulate the optical susceptibility, thus the energy band of specimen[33]. After subtracting the exponential transition, the kinetic trace of recorded transmission shows prominent oscillations comprising two oscillatory components, which last more than 10 ps, as depicted in Fig. 3a, b. The Fourier transform yields a strong peak at 5.16 THz and a weak peak at 0.19 THz, as depicted in Fig. 3c. The former is contributed by the A_{1g} phonons[34] excited through strong electron–phonon coupling at Γ point, dominating the intravalley scattering because of their vanishing momentum. The latter is contributed by the strain wave of breathing mode propagating between the two surfaces of the specimen with a velocity of 2660 m s^{-1}, which agrees with the theoretically predicted 2800 m s^{-1}[35].

Given that only the fully symmetric mode is excited and 2H-$MoTe_2$ absorbs well the laser pulses of 400 nm, the displacive excitation is probably the dominant mechanism for coherent phonon generation, as in other TMDCs[36], in which the oscillation amplitude reaches the maximum in the first period. The observed A_{1g} signal in Fig. 3b takes at least 4 periods to reach the maximum, suggesting new emissions of coherent A_{1g} during the carrier relaxation. We speculated that the intravalley scattering maintains

in-phase during the phonon cascade, leading to the amplification of A_{1g} oscillation. Such a picture is supported by the reported longer periods needed for coherent phonons to reach the maximum amplitude at lower temperature, due to the suppression of the dephasing effect induced by thermal motions[37]. The measured 776 fs of 4 periods is very close to the 0.8 ps of intravalley scattering in the PIB-C decay, setting up the lower bound of time span for the dephasing surpassing the coherent emissions. At this point Eqs. (1) and (2) yield a phonon absorption rate 0.8 times the emission rate, giving rise to the phonon bottleneck. Considering the carrier density injected by excitation, the population of A_{1g} is far more than 4. We simulated the transmittance changes induced by A_{1g} vibration through calculating the relative permittivity changes with the transient structures[36], finding the transmittance changes are linearly proportional to the separation changes of Te atom pairs, as depicted in Fig. 3d. The population of A_{1g} is in turn calculated using the harmonic oscillator model, yielding a value of $\sim 1.87 \times 10^7$ (see Supplementary Note 2). The estimated N_p far more than 1 suggests a substantial optical phonon bottleneck, which may facilitate the higher-order coupling within carriers, e.g., carrier multiplication[38].

A long lifetime of A_{1g} is obtained by the analysis of continuous wavelet transform (CWT), as shown in the inset of Fig. 3c. We extracted the amplitude of CWT, finding that A_{1g} decays through a two-stage process, as depicted in Fig. 3e. The dephasing of coherent phonons includes the processes of pure dephasing and population decay[39], involving changes of only momenta in the former (elastic scattering), and of both momenta and energies in the latter (anharmonic processes, e.g., three-phonon interactions). Thus, we assigned the fast decay (less than 0.3 ps) to the pure dephasing, while the slow one with characteristic time of ~10 ps to the population decay. With the fluence dependent measurements and the inclusion of common Klemens channel[40], a linear dependence of anharmonic rate on the population of lower-frequency acoustic phonons is obtained, as depicted in Fig. 3f. Such a linearity testifies the anharmonicity in the slow decay process, see Supplementary Note 2 for details. The slow relaxation of A_{1g} facilitates the phonon reabsorption by carriers, again corroborating the picture of phonon bottleneck.

Phonon dynamics from Brillouin zone center to border

More phonon dynamics are encoded in the lattice responses captured by UED (see Methods), as the phonon populations alter the scattering of probe electrons. The intensity kinetics of recorded Bragg spots of the FS and CS specimens are depicted in Fig. 4a, showing decay processes with four and three stages, respectively. The FS specimen first undergoes two sequential decays with characteristic times of ~2 ps and ~30 ps, respectively, in which the relative intensity changes follow the Debye–Waller description[41], as depicted in Fig. 4b, indicating the lattice thermalization. During the next ~100 ps, the FS specimen reaches a quasi-thermal-equilibrium, demonstrating the process of phonon–phonon scattering among different modes. Note that the phonons captured in UED exclude the A_{1g} mode, which vibrates parallel to the propagation direction of probe electron beam. A third intensity decay of ~900 ps follows the quasi-equilibrium, suggesting an extra thermalization process. We attributed this long decay to the nonradiative recombination of band-edge excitons, which was also detected in the carrier relaxation with similar timescale depicted in Fig. 2a. At last, the lattice begins to cool down after 2 ns of heating up, indicated by the intensity recovery in ~4 ns (limited by the time window of measurement). The CS specimen undergoes two similar intensity decays of ~2 ps and ~20 ps, followed by a lattice cooling of ~700 ps. The accelerated thermalizing and cooling processes demonstrate the phonon coupling across the heterostructure interface, see Supplementary Note 3 and 4 for further discussions.

Addition to the accelerated rates, the amplitude of first decay in the CS specimen (8.3%) is apparently less than that in the FS specimen (13.1%), indicating the decreased population of SCPs due to the extra dissipation channels provided by the substrate. We thus conclude that the acoustic SCPs, besides the A_{1g}, also populate and reach a non-equilibrium distribution in the excited 2H-$MoTe_2$, because the group velocity of OPs in the 2H-$MoTe_2$ film is too slow to directly couple to the phonons in substrate[26]. Taking the quasi-ballistic effect and the thermal boundary resistance into account, we deduced a thermal boundary conductance of ~10 MW m^{-2} K^{-1}, which is close to the value of MoS_2 film with SiO_2 substrate[42], well modeling the experimental conditions, see Supplementary Note 4 for details.

Acoustic SCPs at the *M* and *K* points of BZ dominating the ultrafast lattice disorder are reported in other TMDCs[18,43]. In the description of electron-phonon coupling with structured susceptibility, SCPs arise from the wavevector-dependent coupling vertex[44], because they correspond to the inelastic scattering and the disappearance of Fermi surface nesting in bulk 2H-$MoTe_2$, see Supplementary Note 5 for further discussions. The larger coupling constant of longitudinal APs at the *M* point (LAPs-M) compared to those of other acoustic modes is revealed by the simulation for 2H-$MoTe_2$[11]. So that we believe the first intensity decay is majorly contributed from the population of LAPs-M, which follows the Debye–Waller relationship[45]. The populations in FS and CS specimens are estimated to be $\sim 8 \times 10^{12}$ and $\sim 5 \times 10^{12}$, respectively (see Supplementary Note 6), suggesting the occurrence of phonon bottleneck of LAPs-M.

Compared to the Bragg scattering encoding the momenta transferred from reciprocal vectors, the signals of diffuse scattering encode the momenta transferred from phonons at specific BZ locations[46]. The differential patterns of FS specimen at 2 and 100 ps referred to that before excitation are shown in Fig. 4c, showing diffuse signals in the former barely changed near the reduced Bragg spots (centers of BZ) while increased at other locations. In the latter, the diffuse signals uniformly increased, with further reduction of Bragg spots. The delayed diffuse signal increase at the locations near Bragg spot suggests the stronger electron–phonon coupling at BZ border compared to that near the BZ center, inducing the faster phonon population at locations away from the Γ point. The diffuse signal kinetics at selected locations are depicted in Fig. 4d, representing the phonon dynamics extracted from the high-symmetry points and the locations close to BZ center, as marked in the inset of Fig. 4d. All kinetics show identical fast intensity increases (~3 ps) followed by distinct second processes, which exhibit a trend of intensity change from decrease to increase as the location changing from the BZ border to the center. Such evolutions demonstrate the energy relaxation pathway from hot carriers to SCPs, then to low-frequency phonons.

In TMDCs, interlayer interactions result in the Davydov splitting[47] of acoustic phonon modes, forming the ultralow-frequency region in the phonon spectra. We examined the scattering of LAPs-M in this region. The phonons at locations around *M* points, with the eigenvectors shown in Supplementary Fig. 11, are expected to possess high scattering rates due to the spin texture[48,49]. We estimated the nonequilibrium population of LAPs-M by implementing the variation of first-order diffuse intensity, and excluding the contributions from high frequency phonons and higher-order scattering for their much smaller cross sections. The calculations yielded a lower bound of 54 (see Supplementary Note 7), again suggesting the phonon bottleneck of LAPs-M.

A more detailed diagram of intervalley scattering of carriers and phonons is schematically illustrated in Fig. 4e, showing the phonon emissions around *K* points induced by the electron scattering between opposite Λ valleys, and those around *M* points by the electron scattering between straddling Λ valleys. These phonons are equivalent to those emitted from the Γ point to the BZ border, contributing to the diffuse signals at high-symmetry points. All these intervalley scatterings are involved in the APs emission illustrated in Fig. 2b, dominating the fast intensity decay of Bragg spots.

Discussion

Combining the results of calculation and measurements of TA and UED, we are able to construct a comprehensive picture of energy relaxation after photoexcitation in 2H-$MoTe_2$, as illustrated in Fig. 5. The photoexcited hot carriers decay through intravalley scattering within a subpicosecond duration, accompanied with the emissions of A_{1g} OPs. A part of the hot carriers decay through intervalley scattering within several picoseconds, accompanied with the APs emission preferentially at the BZ border, due to the

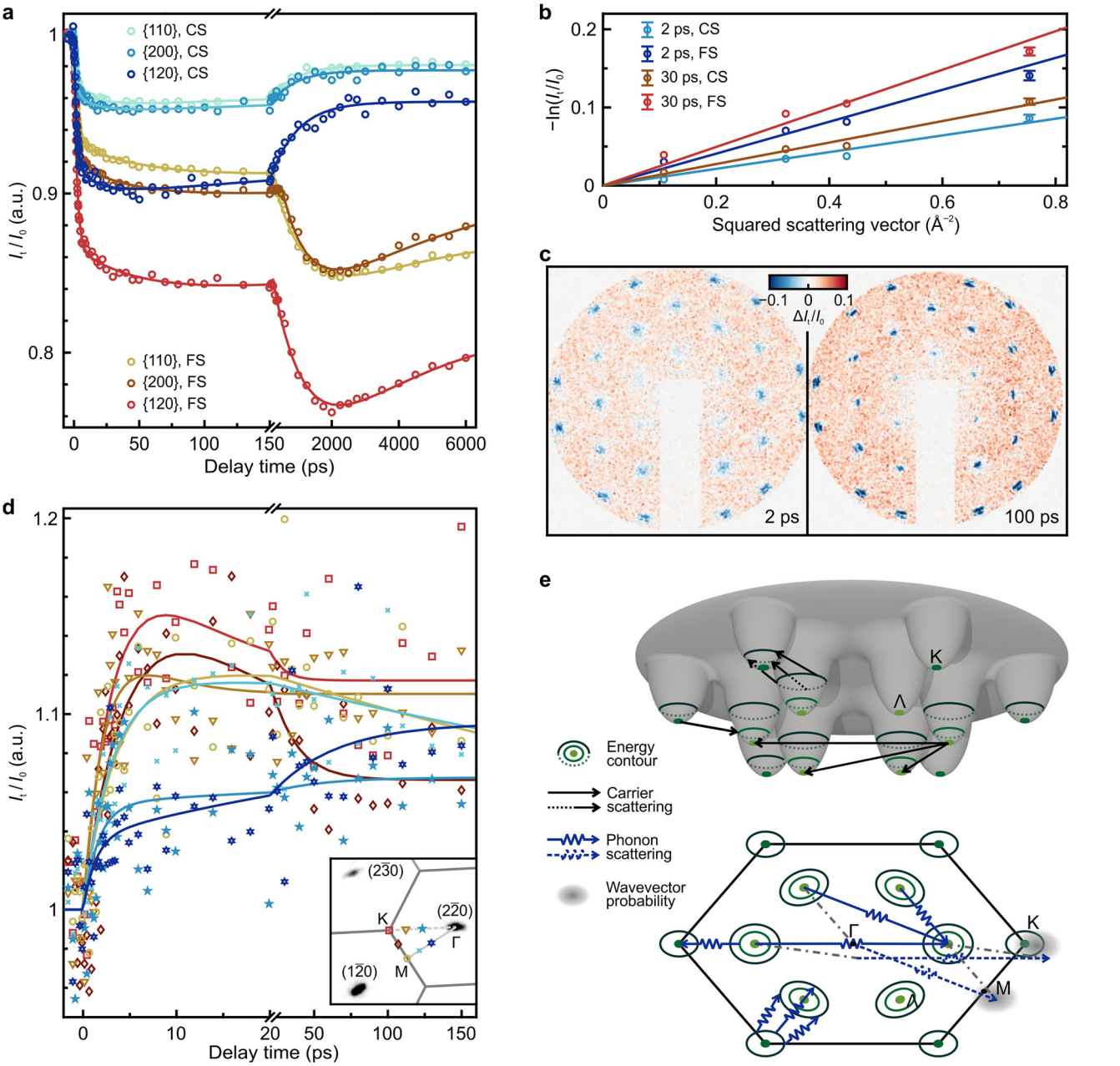

Fig. 4 | Lattice dynamics and intervalley scattering of carriers and phonons. **a** Intensity decay of Bragg spots under excitation of 120 μJ cm^{-2} in the FS and CS specimens. Solid lines, multiexponential fits. **b** Linear dependence of relative intensity changes on squared scattering vector for the first two decays in (**a**). Error bars represent the standard deviation in fitting the measured kinetics. The standard deviations smaller than 0.003 are not displayed for clarity. **c** Differential diffraction patterns of FS specimen at delay times of 2 (left) and 100 (right) ps, referred to the pattern before excitation. Both the increase (red) of diffuse scattering and the decrease (blue) of Bragg scattering indicate the populating phonons. **d** Kinetics of diffuse signal at the selected locations marked in the inset. Note that the low signal-to-noise rate is due to the very low intensity of diffuse scattering (a factor of 10^{-3} compared to the signal of Bragg spots). Solid lines, multiexponential fits. **e** Schematic illustration of intervalley scattering of carriers and phonons in the reduced and projected band structures with six *Λ* and six *K* valleys located with rotational symmetry. Dash-dot lines, the guides to the eye for equivalent transitions.

obstruction in intravalley cooling induced by the phonon bottleneck of A_{1g}. The acoustic SCPs also give rise to the phonon bottleneck at BZ border within a few picoseconds, which is followed by the population of low-frequency phonons in couple tens of picosecond, resulting in the fast disorder of lattice. The FS specimen maintains a quasi-thermal-equilibrium lasting a hundred picoseconds, while the CS specimen cools down several nanoseconds earlier because the substrate effectively drains away the acoustic phonons prior to their equilibrium, therefore alleviates the obstruction of thermal relaxation.

The strong electron–phonon coupling in 2H-$MoTe_2$ is unprofitable for applications utilizing excited carriers, but the phonon bottlenecks and the carrier multiplication provide potentials for the application of hot-carrier solar cell with improving photoelectric conversion efficiency[50]. As either photon or electric field stimulates phonon populations in semiconductors[26], the rich phonon pathways revealed in 2H-$MoTe_2$ also provide potentials for heat management applications.

The implement of ultrafast optical and electron probes, with the advantage of momentum-resolving in the latter, makes possible picking out the information of phonon bottleneck from the shielding effect[51] of electron-phonon coupling, and from the different valleys in band structure. We demonstrate here various approaches to estimate the phonon populations based on the measurements of optical absorption and electron diffraction,

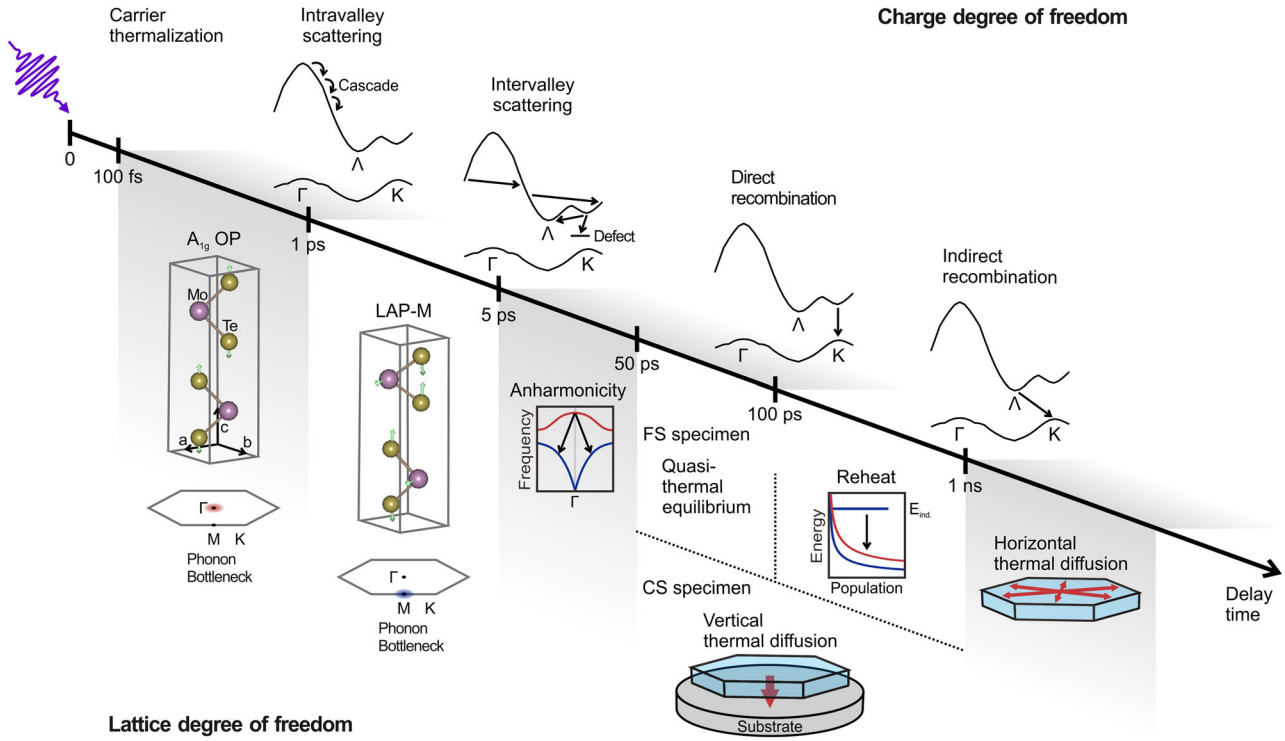

Fig. 5 | Schematic diagram of photoexcited carriers and phonons evolving in 2H-$MoTe_2$ during a time window of nanoseconds. Upon photoexcitation, the carriers thermalize within 100 fs. Subsequently, the hot carriers cool down via intravalley scattering within a picosecond and intervalley scattering within several picoseconds, accompanied with the emissions of A_{1g} OP at the BZ center and APs at the BZ border, respectively. Both the emitted SCPs undergo the phonon bottleneck. Then the anharmonic coupling with SCPs excites the low-frequency phonons in several tens of picosecond. The FS specimen establishes a quasi-thermal-equilibrium and is reheated by the indirect recombination in a duration of one nanosecond, followed by a cooling procedure through thermal diffusion within the specimen, which lasts a few nanoseconds. The heat dissipation in the CS specimen is significantly accelerated due to the thermal diffusion towards the substrate, which finishes in one nanosecond.

quantitatively distinguishing the occurrence of different phonon bottlenecks. At the end, we are able to elucidate the carrier and phonon interactions across the charge, lattice, and valley degrees of freedom on their respective timescales, providing a frame for better understanding this highly complex scenario, and hopefully for harnessing these processes in valleytronics and other optoelectronic applications.

Methods

Specimen preparation

The Mo film deposited on a 1-in. Si/SiO_2 wafer through magnetron sputtering was tellurized with Te vapor in a horizontal hot-wall tube furnace (at ~510 °C) to obtain a polycrystalline 1T′-$MoTe_2$ film. A seed single-crystalline 2H-$MoTe_2$ nano-flake, mechanically exfoliated from the bulk crystal, was dryly transferred on the 1T′-$MoTe_2$ film. After that, an Al_2O_3 layer was deposited on the surface by atomic layer deposition, and a small hole through 2H- and 1T′-$MoTe_2$ was punched by a tungsten probe mounted on a 3D translation stage. The wafer and a 3-g Te lump were placed in a closed quartz tube and then loaded into another quartz tube in a chemical vapor deposition furnace. The 1T′-$MoTe_2$ layer underneath the seed crystal transformed into a 2H-$MoTe_2$ single crystal through the phase transition and recrystallization induced by interface at ~650 °C. At last, the Al_2O_3 layer was dissolved using a hot phosphoric acid solution. After etching the Si/SiO_2 substrate by hydrogen fluoride, the 2H-$MoTe_2$ film can float on liquid level. Then the copper grids, bare or coated with ultrathin amorphous carbon membrane (with mean thickness of ~8.5 nm), were used to attach the 2H-$MoTe_2$ films as FS and CS specimens, as shown in Fig. 1a. More details can be found in the earlier report[19]. The atom-resolved structure and crystallization of the obtained specimens are characterized by the electron imaging and diffraction, as shown in Supplementary Fig. 1.

Density functional theory (DFT) calculation

The calculations of geometry optimization (see Supplementary Data 1), electronic band structure, optical properties, and Fermi surface were performed using DFT within the Vienna Ab initio Simulation Package (VASP) code[52] with the generalized gradient approximation of Perdew–Burke–Ernzerhof (GGA–PBE). The projected augmented wave method was utilized with a plane-wave basis set[53,54], with the convergence criteria set to 10^{-5} eV for energy and 0.01 eV $Å^{-1}$ for force. A kinetic cutoff energy of 500 eV and a Monkhorst–Pack[55] special k-point mesh of $5 \times 5 \times 1$ were employed for calculations. Additionally, the DFT-D3 method developed by Grimme was employed to account for the van der Waals interactions[55]. The vibrational properties are obtained from the density functional perturbation theory using the Phonopy code[56] and a 4×4 supercell.

Non-adiabatic molecular dynamics (NAMD)

The Hefei-NAMD code[57,58] was employed for the NAMD simulation. The relaxation of photoexcited carriers was modeled using the decoherence-induced surface hopping method, within the framework of time-dependent density functional theory in the Kohn–Sham (KS) scheme[59]. Prior to conduct the NAMD calculations, the adiabatic molecular dynamics (MD) simulations were performed with an orthogonal 3×3 supercell, consisting of a total of 108 atoms. The structure was fully relaxed at 0 K, then heated to 300 K over a period of 1 ps using repeated velocity rescaling. Following the heating phase, an adiabatic MD trajectory of 5 ps was generated in the microcanonical ensemble (NVE) with a nuclear time step of 1 fs. The nonadiabatic coupling matrix elements were computed along the trajectory. To simulate the electron/hole dynamics, 200 initial configurations were selected from the final 3 ps of the trajectory. The initial and final atomic coordinates are supplied in Supplementary Data 2 and 3, respectively.

Transient absorption spectroscopy

The TA measurements were performed under the ambient atmosphere using a Helios spectrometer (Ultrafast Systems), and a Ti:sapphire regenerative amplifier (Legend, Coherent) which delivers pulses of 800 nm, with pulse width of 40 fs and repetition rate of 5 kHz. The repetition rate was chopped to 2.5 kHz in measurements. The output from the regenerative amplifier was divided into two arms by a beam splitter. One arm was used for the second harmonic generation from a BaB_2O_4 (BBO) crystal to excite the specimen, so that the 3.1 eV photons drove the population of hot carriers and the subsequent carrier multiplication. The other arm was used for the generation of white-light continuum (Ti:sapphire for 400–800 nm, Nd:YAG for 850–1450 nm) as the probe pulses. The diameter of pump and probe spots were 200 μm and 100 μm, respectively. The instrument response function was measured as ~100 fs.

Single-wavelength transient absorption measurement

The specimen was excited with the same conditions as the TA measurement, and probed by the fundamental output of 800 nm from the Ti:sapphire regenerative amplifier. The repetition rate was chopped to 125 Hz in measurements. A silicon detector (DET36A/M, Thorlabs) was used to record the transmitted light, then the signals were amplified by a lock-in amplifier (SR865, Stanford Research Systems).

Ultrafast electron diffraction

The UED measurements were performed under the ultrahigh vacuum condition using a home-built ultrafast electron diffractometer with estimated temporal resolution of subpicosecond[60], and the same Ti:sapphire regenerative amplifier as the TA measurement. The specimen was also excited with 400 nm pulses. The pulsed probe electrons were accelerated by an electric field of 30 kV, generating diffraction patterns through a transmission geometric setup. The diffraction signals were gained by two chevron-stack microchannel plates, then recorded by a CMOS camera (ORCA-Flash, Hamamatsu). Each pattern was recorded with 15,000 accumulated pulses. The diameter of pump and probe spots were ~700 μm and ~100 μm, respectively. The intensity of Bragg spots presented in the manuscript is averaged over all recorded spots of the same family.

Data availability

The data that support the findings of this study are available from the corresponding author upon request.

Received: 4 April 2025; Accepted: 8 August 2025;
Published online: 23 August 2025

References

1. Deng, Y. et al. $MoTe_2$: semiconductor or semimetal?. *ACS Nano* **15**, 12465–12474 (2021).
2. Chen, J. et al. Quantum effects and phase tuning in epitaxial hexagonal and monoclinic $MoTe_2$ monolayers. *ACS Nano* **11**, 3282–3288 (2017).
3. Qi, Y. et al. Superconductivity in weyl semimetal candidate $MoTe_2$. *Nat. Commun.* **7**, 11038 (2016).
4. Deng, K. et al. Experimental observation of topological Fermi arcs in type-II Weyl semimetal $MoTe_2$. *Nat. Phys.* **12**, 1105–1111 (2016).
5. Empante, T. A. et al. Chemical vapor deposition growth of few layer $MoTe_2$ in the 2H, 1T′, and 1T phases: tunable properties of $MoTe_2$ films. *ACS Nano* **11**, 900–905 (2017).
6. Manzeli, S. et al. 2D transition metal dichalcogenides. *Nat. Rev. Mater.* **2**, 17033 (2017).
7. Kim, J. et al. Carrier multiplication in van der Waals layered transition metal dichalcogenides. *Nat. Commun.* **10**, 5488 (2019).
8. Shin, D. et al. Phonon-driven spin-floquet magneto-valleytronics in MoS_2. *Nat. Commun.* **9**, 638 (2018).
9. Maiti, R. et al. Strain-engineered high-responsivity $MoTe_2$ photodetector for silicon photonic integrated circuits. *Nat. Photon.* **14**, 578–584 (2020).
10. Wang, Y. et al. Structural phase transition in monolayer $MoTe_2$ driven by electrostatic doping. *Nature* **550**, 487–491 (2017).
11. Krishnamoorthy, A. et al. Optical control of non-equilibrium phonon dynamics. *Nano Lett.* **19**, 4981–4989 (2019).
12. Britz, A. et al. Carrier-specific dynamics in 2H-$MoTe_2$ observed by femtosecond soft x-ray absorption spectroscopy using an X-ray free-electron laser. *Struct. Dyn.* **8**, 014501 (2021).
13. Attar, A. R. et al. Simultaneous observation of carrier-specific redistribution and coherent lattice dynamics in 2H-$MoTe_2$ with femtosecond core-level spectroscopy. *ACS Nano* **14**, 15829–15840 (2020).
14. Chi, Z. et al. Ultrafast carrier and phonon dynamics in few-layer 2H-$MoTe_2$. *J. Chem. Phys.* **151**, 114704 (2019).
15. Hu, X. et al. Structural regulation and application of transition metal dichalcogenide monolayers: progress and challenges. *Coord. Chem. Rev.* **499**, 215504 (2024).
16. Stoneham, A. M. Non-radiative transitions in semiconductors. *Rep. Prog. Phys.* **44**, 1252–1295 (1981).
17. Fukuda, T. et al. Photo-induced tellurium segregation in $MoTe_2$. *Phys. Status Solidi RRL* **16**, 2100633 (2022).
18. Lin, M. F. et al. Ultrafast non-radiative dynamics of atomically thin $MoSe_2$. *Nat. Commun.* **8**, 1745 (2017).
19. Xu, X. et al. Seeded 2D epitaxy of large-area single-crystal films of the van der Waals semiconductor 2H $MoTe_2$. *Science* **372**, 195–200 (2021).
20. Kresse, G. & Furthmüller, J. Efficiency of ab-initio total energy calculations for metals and semiconductors using a plane-wave basis set. *Comput. Mater. Sci.* **6**, 15–50 (1996).
21. Jung, E. et al. Unusually large exciton binding energy in multilayered 2H-$MoTe_2$. *Sci. Rep.* **12**, 4543 (2022).
22. Wang, W. et al. Investigation of hot carrier cooling dynamics in monolayer MoS_2. *J. Phys. Chem. Lett.* **12**, 861–868 (2021).
23. Paradisanos, I. et al. Efficient phonon cascades in WSe_2 monolayers. *Nat. Commun.* **12**, 538 (2021).
24. Martin, R. M. & Varma, C. M. Cascade theory of inelastic scattering of light. *Phys. Rev. Lett.* **26**, 1241–1244 (1971).
25. Shi, H. et al. Exciton dynamics in suspended monolayer and few-layer MoS_2 2D Crystals. *ACS Nano* **7**, 1072–1080 (2013).
26. Ferry, D. K. Non-equilibrium longitudinal optical phonons and their lifetimes. *Appl. Phys. Rev.* **8**, 021324 (2021).
27. Li, Y. et al. Slow cooling of high-energy C excitons is limited by intervalley-transfer in monolayer MoS_2. *Laser Photon. Rev.* **13**, 1800270 (2019).
28. Din, N. U., Turkowski, V. & Rahman, T. S. Ultrafast charge dynamics and photoluminescence in bilayer MoS_2. *2d Mater.* **8**, 025018 (2021).
29. Kumar, N., He, J. Q., He, D. W., Wang, Y. S. & Zhao, H. Charge carrier dynamics in bulk MoS_2 crystal studied by transient absorption microscopy. *J. Appl. Phys.* **113**, 133702 (2013).
30. Raja, A. et al. Enhancement of exciton-phonon scattering from monolayer to bilayer WS_2. *Nano Lett.* **18**, 6135–6143 (2018).
31. Froehlicher, G., Lorchat, E. & Berciaud, S. Direct versus indirect band gap emission and exciton-exciton annihilation in atomically thin molybdenum ditelluride ($MoTe_2$). *Phys. Rev. B* **94**, 085429 (2016).
32. Li, Y., Wu, X., Liu, W., Xu, H. & Liu, X. Revealing the interrelation between C- and A-exciton dynamics in monolayer WS_2 via transient absorption spectroscopy. *Appl. Phys. Lett.* **119**, 051106 (2021).
33. Zhang, M. et al. light-induced subpicosecond lattice symmetry switch in $MoTe_2$. *Phys. Rev. X* **9**, 021036 (2019).
34. Froehlicher, G. et al. Unified description of the optical phonon modes in *N*-Layer $MoTe_2$. *Nano Lett.* **15**, 6481–6489 (2015).

35. Rivas, N. et al. Generation and detection of coherent longitudinal acoustic waves in ultrathin 1T'-$MoTe_2$. *Appl. Phys. Rev.* **115**, 223103 (2019).
36. Trovatello, C. et al. Strongly coupled coherent phonons in single-layer MoS_2. *ACS Nano* **14**, 5700–5710 (2020).
37. Jeong, T. Y. et al. Coherent lattice vibrations in mono- and few-layer WSe_2. *ACS Nano* **10**, 5560–5566 (2016).
38. Ellingson, R. J. et al. Highly efficient multiple exciton generation in colloidal PbSe and PbS quantum dots. *Nano Lett.* **5**, 865–871 (2005).
39. Lee, Y. J., Parekh, S. H., Fagan, J. A. & Cicerone, M. T. Phonon dephasing and population decay dynamics of the G-band of semiconducting single-wall carbon nanotubes. *Phys. Rev. B* **82**, 165432 (2010).
40. Klemens, P. G. Anharmonic decay of optical phonons. *Phys. Rev.* **148**, 845–848 (1966).
41. Schäfer, S., Liang, W. & Zewail, A. H. Structural dynamics of nanoscale gold by ultrafast electron crystallography. *Chem. Phys. Lett.* **515**, 278–282 (2011).
42. Yalon, E. et al. Energy dissipation in monolayer MoS_2 electronics. *Nano Lett.* **17**, 3429–3433 (2017).
43. Caruso, F. Nonequilibrium lattice dynamics in monolayer MoS_2. *J. Phys. Chem. Lett.* **12**, 1734–1740 (2021).
44. Otto, M. R. et al. Mechanisms of electron-phonon coupling unraveled in momentum and time: the case of soft phonons in $TiSe_2$. *Sci. Adv.* **7**, abf2810 (2021).
45. Schäfer, S., Liang, W. & Zewail, A. H. Primary structural dynamics in graphite. *N. J. Phys.* **13**, 063030 (2011).
46. de Cotret, L. P. R. et al. Time- and momentum-resolved phonon population dynamics with ultrafast electron diffuse scattering. *Phys. Rev. B* **100**, 214115 (2019).
47. Song, Q. J. et al. Physical origin of Davydov splitting and resonant Raman spectroscopy of Davydov components in multilayer $MoTe_2$. *Phys. Rev. B* **93**, 115409 (2016).
48. Waldecker, L. et al. Momentum-resolved view of electron-phonon coupling in multilayer WSe_2. *Phys. Rev. Lett.* **119**, 036803 (2017).
49. Bertoni, R. et al. Generation and evolution of spin-, valley-, and layer-polarized excited carriers in inversion-symmetric WSe_2. *Phys. Rev. Lett.* **117**, 277201 (2016).
50. Tsai, C.-Y. Carrier heating and its effects on the current-voltage relations of conventional and hot-carrier solar cells: a physical model incorporating energy transfer between carriers, photons, and phonons. *Sol. Energy* **188**, 450–463 (2019).
51. Zhu, H. et al. Screening in crystalline liquids protects energetic carriers in hybrid perovskites. *Science* **353**, 1409–1413 (2016).
52. Kresse, G. & Hafner, J. Ab initio molecular dynamics for liquid metals. *Phys. Rev. B* **47**, 558–561 (1993).
53. Blöchl, P. E. Projector augmented-wave method. *Phys. Rev. B* **50**, 17953–17979 (1994).
54. Kresse, G. & Furthmüller, J. Efficient iterative schemes for ab initio total-energy calculations using a plane-wave basis set. *Phys. Rev. B* **54**, 11169–11186 (1996).
55. Grimme, S., Antony, J., Ehrlich, S. & Krieg, H. A consistent and accurate ab initio parametrization of density functional dispersion correction (DFT-D) for the 94 elements H-Pu. *J. Chem. Phys.* **132**, 154104 (2010).
56. Togo, A. First-principles Phonon Calculations with Phonopy and Phono3py. *J. Phys. Soc. Jpn***92**, 012001 (2023).
57. Zheng, Z., Zheng, Q. & Zhao, J. Ultrafast electron transfer dynamics in lateral transition-metal dichalcogenide heterostructures. *Electron. Struct.* **1**, 034001 (2019).
58. Zheng, Q. et al. Phonon-assisted ultrafast charge transfer at van der Waals heterostructure interface. *Nano Lett.* **17**, 6435–6442 (2017).
59. Jaeger, H. M., Fischer, S. & Prezhdo, O. V. Decoherence-induced surface hopping. *J. Chem. Phys.* **137**, 22A545 (2012).
60. Hu, C. L., Wang, Z., Shi, Y. J., Ye, C. & Liang, W. X. Design of an ultrafast electron diffractometer with multiple operation modes. *Chin. Phys. B* **30**, 090701 (2021).

Acknowledgements

Z.W. and C.H. thank the financial support from the National Natural Science Foundation of China (62474073). We thank Dr. Z.X. for the helps on DFT calculations.

Author contributions

W.L. conceived of and supervised the project. Z.W. performed the measurements with supports from Y.S., X.W., Z.Z., X.Z., F.H., Q.Y., and C.H. Y.P synthesized the 2H-$MoTe_2$ films under supervisions from Y.Y. M.L. performed the NAMD simulation under supervisions from J.H. Z.W., and W.L. analyzed the data with discussions with all authors. Z.W. and W.L. wrote the paper with contributions from all authors.

Competing interests

The authors declare no competing interests.

Additional information

Supplementary information The online version contains supplementary material available at https://doi.org/10.1038/s42005-025-02267-y.

Correspondence and requests for materials should be addressed to Wenxi Liang.

Peer review information *Communications Physics* thanks the anonymous reviewers for their contribution to the peer review of this work.